World Electric Vehicle Journal

MDPI

Article

Improvement on Electromagnetic Performance of Axial–Radial Flux Type Permanent Magnet Machines by Optimal Stator Slot Number

Ran Yi, Chunwei Yuan, Hongbo Qiu, Wenhao Gao and Junyi Ren *

College of Electrical and Information Engineering, Zhengzhou University of Light Industry, Zhengzhou 450000, China; yiranjob@163.com (R.Y.); 3322010100005@email.zzuli.edu.cn (C.Y.); qiuhongbo@zzuli.edu.cn (H.Q.); 332101050077@email.zzuli.edu.cn (W.G.)
* Correspondence: renjunyi60@gmail.com

Abstract: To achieve the objective of high torque, a high utilization rate of PMs, and flexible flux regulation capability of the permanent magnet (PM) machine, an axial–radial flux type permanent magnet (ARFTPM) machine was studied in this paper. The working principle of the ARFTPM machine is analyzed by illustrating the flux paths. Then, the influence of stator slot number on the flux regulation capability and torque is studied. A full comparison of the main parameters and electromagnetic performances of the ARFTPM machine with different stator slot numbers is presented, including winding coefficient, back electromotive force (EMF), cogging torque, average torque, and torque-angle characteristics. The optimal stator slot number was obtained. Finally, the 12-slot/10-pole prototype machine is manufactured and tested to validate the simulation data and theoretical analysis.

Keywords: permanent magnet motor; flux regulation capability; parallel magnetic path; back-EMF

check for updates

Citation: Yi, R.; Yuan, C.; Qiu, H.; Gao, W.; Ren, J. Improvement on Electromagnetic Performance of Axial–Radial Flux Type Permanent Magnet Machines by Optimal Stator Slot Number. *World Electr. Veh. J.* **2024**, *15*, 535. https://doi.org/10.3390/wevj15110535

Academic Editor: Michael Fowler

Received: 17 October 2024
Revised: 5 November 2024
Accepted: 16 November 2024
Published: 19 November 2024

Copyright: © 2024 by the authors. Published by MDPI on behalf of the World Electric Vehicle Association. Licensee MDPI, Basel, Switzerland. This article is an open access article distributed under the terms and conditions of the Creative Commons Attribution (CC BY) license (https://creativecommons.org/licenses/by/4.0/).

1. Introduction

Permanent magnet (PM) machines are widely used in aerospace, electric vehicles, industrial transportation, and wind power generation due to their high efficiency and high torque density. However, due to the single excitation source in the PM machines, the air gap magnetic field is difficult to regulate. Furthermore, the speed regulation range of the motor and the voltage regulation capabilities of the generator are also limited [1–4].

At present, new types of machines with a wide speed regulation range are being explored by many experts. According to the magnetic field regulation mode, the regulating device can be divided into hybrid excitation motors [5], variable leakage flux motors [6], winding switching motors [7], and memory motors [8]. Hybrid excitation (HE) machines are a combination of permanent magnet magnetomotive force (MMF) and electric excitation MMF. The HE machines' cost is low, and they integrate the advantages of the PM machines and the excellent flux regulation capability [9–12]. Due to the added electric excitation MMF, the flux regulation capability is improved. However, the machine design and control system are more challenging [13,14].

The HE machines' topologies are diverse. Based on the coupling relationship of the permanent magnetic circuit and the electric excitation magnetic circuit, the HE machines can be divided into two groups: (1) the series HE machines and (2) the parallel HE machines. The series HE machines originate from the conventional PM machines, while the field excitation coils (FCs) are located on the stator [15]. It should be noted that since the radial magnetic circuit is in series, the electric excitation flux will pass through the PMs, which could limit the machine flux regulation capability and increase the risk of irreversible demagnetization of the PMs. In addition to the radial magnetic circuit, the axial magnetic circuit of the HE machines can also be used as the flux path of the electric excitation

source. Consequently, the ARFTPM machine is proposed, in which the axial magnetic circuit is composed of N- and S-pole magnetic rings, a field excitation coil, and an end cap. Compared with conventional series HE machines, the space utilization and hence the electromagnetic performance can be improved significantly. Moreover, in the process of motor design, selecting the appropriate pole slot combination can enhance the performance of the motor. The influence of various slot/pole number combinations has not been systematically discussed for the axial–radial permanent magnet motor with flexible flux regulation capability.

In this paper, the 3-D models of the ARFTPM machines are established based on the finite-element analysis (FEA). The machine topology and basic operating principle are studied by illustrating the flux paths. A full comparison of the main parameters and electromagnetic performance indexes of the ARFTPM machine is presented, including winding coefficient, back electromotive force (EMF), cogging torque, average torque, and torque-angle characteristics. The influence of stator slot numbers on the flux regulation capability and torque is studied. Combined with the Fourier decomposition method, the harmonic variations in the ARFTPM machines are analyzed. Finally, the simulation data and theoretical analysis are verified by experiments.

2. Machine Topologies and Operating Principle

It can be seen in Figure 1 that the 3-D FEA structural section of the ARFTPM machine is established to perform the analysis of field distribution. The rotor is composed of tangential PMs and radial PMs alternately. The bonded neodymium-based magnet, grade N35, is used as the material for all PMs. The part of the air gap between the rotor and stator is the radial air gap, which is 0.5 mm. To improve the flux regulation capability of the ARFTPM machine, a double-ended excitation structure is adopted. The FCs are embedded in the annular groove inside the end cap and located outside the magnetic ring. The magnetic rings are outside the rotor and rotate synchronously with it. To generate the axial magnetic shunt of the rotor, the N- and S-pole magnetic rings are fabricated by tungsten steel M20, which has strong mechanical strength and excellent magnetic permeability.

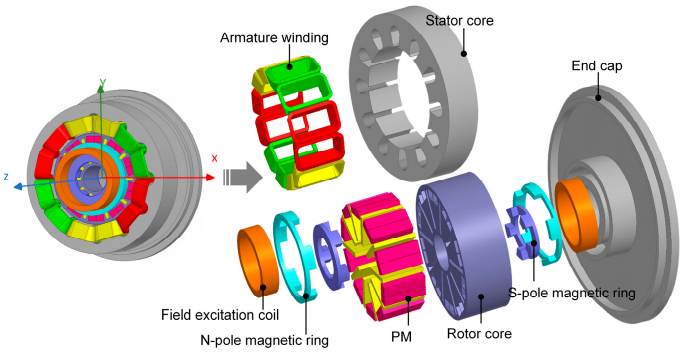


Figure 1. Lateral and front view of the FTRHEM.

To demonstrate the operating principle of the ARFTPM machine, the flowing paths of the PM flux and the axial MMF flux are depicted in Figure 2. As shown in Figure 2a, the PM flux originates from the rotor and reaches the stator after passing through the radial air gap. Also, the axial magnetic leakage flux path is shown in Figure 2b. A part of the PM flux passes through the axial air gap, rotor, and the N-pole magnetic ring, then passes through the ferromagnetic bridge to complete the closed loop through the S-pole magnetic ring. Due to the PM flux leaking by the axial magnetic shunt (b), the main air gap flux is weakened.

As shown in Figure 2c, when the negative axial MMF is generated by the FCs, the magnetic flux passes through the ferromagnetic bridge, air gap, S-pole magnetic ring, rotor, radial air gap, stator, rotor, axial air gap, N-pole magnetic ring, and finally returns to the ferromagnetic bridge. The axial part direction of the magnetic circuit (c) and the path (b) are

the same, and thus the air gap flux of the ARFTPM machine can be reduced by negative axial MMF. In addition, the flux-enhancing is shown in Figure 2d; its axial part is opposite to the path (b) with positive axial MMF, so the air gap flux of the machine can be increased with the positive axial MMF. To sum up, the magnetic flux can be adjusted by the FCs.

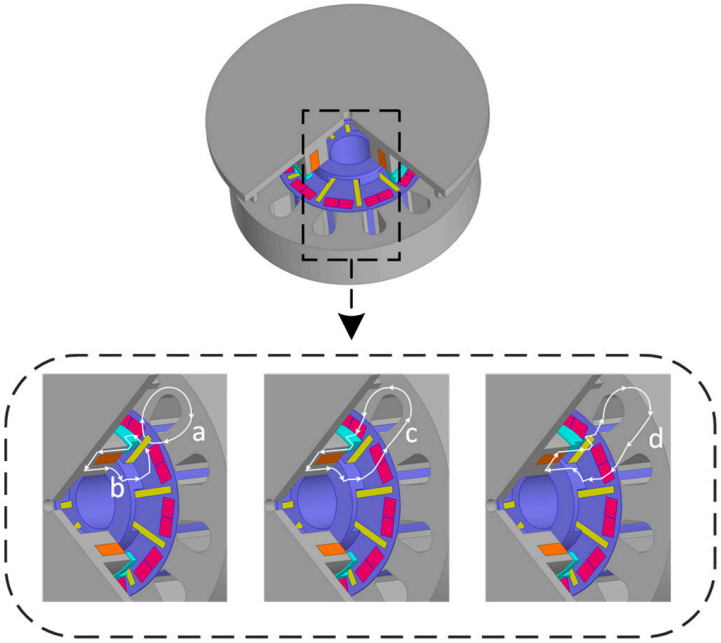


Figure 2. Illustration of flux paths for PMs and axial MMF (**a**) radial magnetic flux; (**b**) axial magnetic flux; (**c**) flux-wakening; and (**d**) flux-enhancing.

The resultant phase flux linkage of the ARFTPM machine in the d-q coordinate ψ_d can be expressed as [5]

$$\psi_d = \psi_{PM} + L_d i_d + M_{df} i_f \quad (1)$$

where ψ_{PM}, L_d, M_{df} represent the PM flux linkage, d-axis synchronous inductance, and mutual inductance between armature coils and FCs, while i_d and i_f are the d-axis armature current and field current, respectively. As a result, the resultant air-gap flux density and thus the phase flux linkage can be regulated in the ARFTPM machine.

The open-circuit phase flux linkages with different axial MMFs are illustrated in Figure 3, in which the results with positive axial MMF, without axial MMF, and negative axial MMF are all included. It can be observed that the flux linkage amplitude is boosted with positive axial MMF, and it is reduced with negative axial MMF. As a result, the resultant air-gap flux density and thus the air-gap flux can be regulated in the ARFTPM machine.

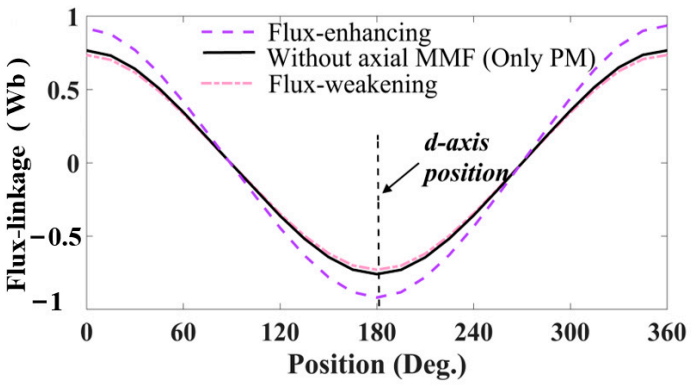


Figure 3. Schematic diagram of no-load flux linkage waveforms with different axial MMF.

3. Winding Configuration and Winding Factor

Similarly to the conventional PM machines, the relationship between the electrical angle θ_e and the rotor mechanical position θ_m is as follows:

$$\theta_e = N_r \theta_m \tag{2}$$

where N_r is the number of rotor pole pairs. The pole-slot combination is flexible in the fractional-slot concentrated windings machine. For this 10-pole structure, the 9-slot, 12-slot, and 15-slot are all feasible according to the pole-slot combination constraints for fractional slot centralized windings. Winding layouts and phasors of the ARFTPM machines are shown in Figure 4, based on which the armature winding configurations can be specified.

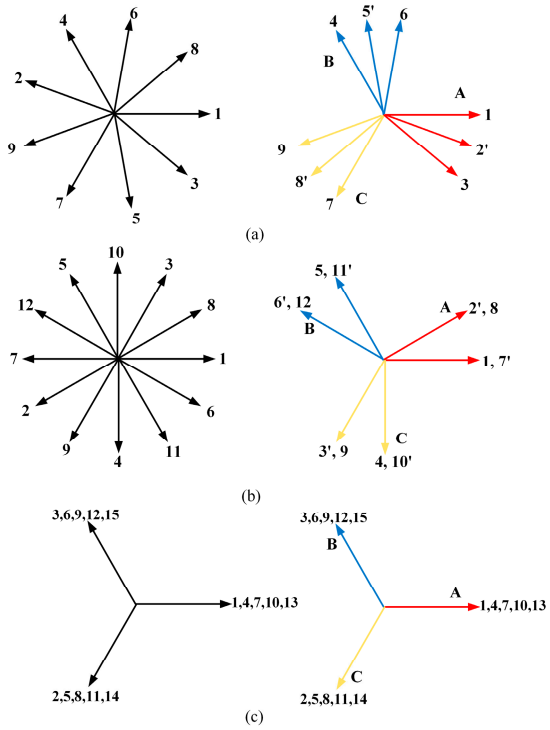


Figure 4. Winding layouts and phasors of ARFTPM machines (**a**) 9-slot; (**b**) 12-slot; and (**c**) 15-slot.

The slot number of the ARFTPM machine has a significant impact on the winding factor K_{wp}. The higher K_{wp} results in higher magnet usage efficiency, and thus the power density can be improved. As shown in Table 1, the distribution factors of machines are almost the same and close to 1; the distribution factor of the 15-slot machine is 1.

Table 1. Winding factors and least common multiple (LCM) of poles and slots of ARFTPM machines with different slot numbers.

Parameter	9-Slot	12-Slot	15-Slot
K_{qp}	0.9598	0.9659	1
K_{yp}	0.9848	0.9659	0.866
$K_{wp} = K_{qp} \cdot K_{yp}$	0.9452	0.933	0.866
LCM	90	60	30

The conventional integer-slot winding factor formula cannot be directly used for the fractional-slot concentrated winding machines. The winding factor K_{wp} for the fractional-slot windings can be expressed as [16]

$$\mathrm{q} = \mathrm{b} + \frac{\mathrm{c}}{d} = \frac{bd + c}{d} \tag{3}$$

$$\begin{cases} \tau = \frac{z}{2p} = mq \\ \beta = \frac{y}{\tau} \end{cases} \tag{4}$$

$$\begin{cases} K_{qp} = \frac{0.5}{(bd+c)\sin\frac{30^\circ}{(bd+c)}} \\ K_{yp} = \sin(\beta \cdot 90^\circ) \\ K_{wp} = K_{qp} \cdot K_{yp} \end{cases} \tag{5}$$

where $q = Z/2pm$, Z is the number of stator slots, τ is the polar distance, y is the winding span, concentrated winding span is always 1. K_{qp}, K_{yp}, K_{wp} are the distribution factor, pitch factor, and winding factor of the fractional-slot windings, c/d is an irreducible fraction. In this paper, the comparison results of different slot numbers are obtained according to the pole-slot combination selection table, as shown in Table 1.

The magnetic vectors of the ARFTPM machines are shown in Figure 5. As shown in Figure 5a, the magnetic vector α of the 9-slot ARFTPM machine from the PMs passes through the radial air gap, stator tooth, and returns to the radial air gap, which does not cross-link with the armature winding. Different from the vector α, the magnetic vector β of the 12-slot machine can cross-link with the armature winding, and thus the main air gap magnetic flux can be improved, according to Figure 5b. The magnetic vector δ of the 15-slot machine in Figure 5c could improve the main air gap magnetic flux like vector β.

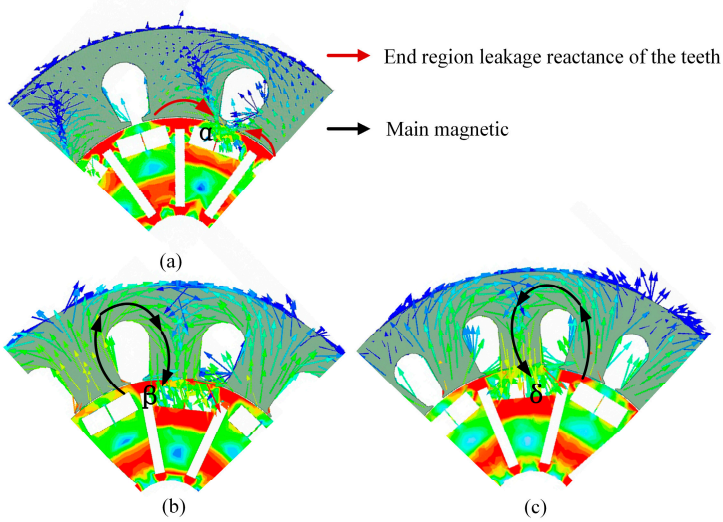


Figure 5. The magnetic vector potential paths of ARFTPM machines. (**a**) 9-slot; (**b**) 12-slot; and (**c**) 15-slot.

In summary, the magnetic vector potential paths of the three machines are various. The main magnetic circuit flux of the 9-slot machine is weakened due to the end region leakage reactance of the stator teeth, which in turn leads to the reduction in back-EMF, and the speed regulation capability of ARFTPM machines is influenced.

To compare the electromagnetic characteristics fairly, the structure parameters of the three machines, such as stator outer diameter, axial length, and air gap, are kept the same. The models were established by the software ANSYS2020R1 with the guarantee of mesh quality. The area of stator teeth, the current density, and the bus voltage of machines are all the same. Meanwhile, the mesh numbers are 140,000, and the time steps are 0.1 ms. In addition, the machine meshing and open-circuit flux density distribution of ARFTPM machines are shown in Figure 6. The stator maximum magnetic flux densities of the three machines are the same. Particularly, the rotor saturation and the magnetic flux leakage between the PM poles of the 12-slot ARFTPM machine are lower than the 9-slot and 15-slot. The finite element setup is set in Table 2.

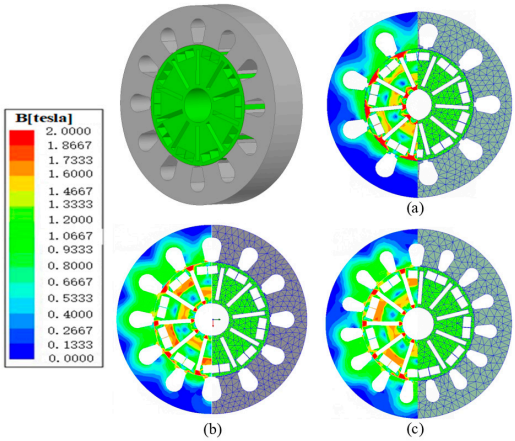


Figure 6. The ARFTPM machine meshing and open-circuit flux density distribution (**a**) 9-slot; (**b**) 12-slot; and (**c**) 15-slot.

Table 2. Values of variables used in the FEA.

Parameters	Value
Calculation step length (s)	0.001
Mesh elements	140,000
Residual value	0.005
Permanent magnet remanent magnetism (T)	1.2
Permanent magnet coercive force (A/m)	−890,000

4. Performance Comparisons

The electromagnetic performance of ARFTPM machines is analyzed and compared by 3-D FEA. The key geometric parameters of machines are shown in Figure 7. Basic parameters of ARFTRM machines is set in Table 3.

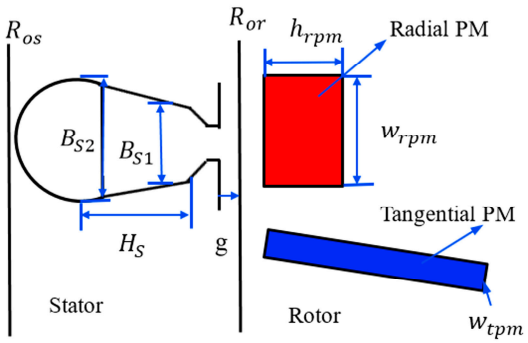


Figure 7. The key geometric parameters of ARFTPM machines.

Table 3. Basic parameters of ARFTRM machines.

Parameters	Value
Rated power (kW)	3.5
Rated speed (r/min)	250
Pole number	10
Air-gap length (mm)	0.5
Radial PM length (mm)	10
Radial PM thickness (mm)	13
Radial PM volume (mm^3)	6500
Tangential PM volume (mm^3)	10,000
Tangential PM length (mm)	40
Tangential PM thickness (mm)	5

It is known that there is a trade-off between torque density and flux regulation capacity in the design of HE machines. The objectives were defined to meet the constraints on split ratio, stack length, and PM usage volume. Since the short-circuit flux can be increased with a thinner air gap, resulting in the sacrificed torque density, and the flux regulation capability can be limited by a thicker air gap, the thickness of the air gap is fixed at 0.5 mm. The peariform slot was usually adopted as the stator slot of the medium and small asynchronous motors. With the constraints of stator inner diameter, stator teeth width, and the yoke height, the slot body bottom width B_{s1} and slot wedge maximum B_{s2} are increased with the reduction in slot number. The structural parameters of the 9-slot, 12-slot, and 15-slot ARFTPM machines are shown in Table 4.

Table 4. Key design parameters of ARFTPM machines.

Parameter	9-Slot	12-Slot	15-Slot
Stator outer radius R_{os} (mm)		115	
Rotor outer radius R_{or} (mm)		69.5	
Air-gap length g (mm)		0.5	
Stator slot number Z	9	12	15
Slot body height H_S (mm)	17.6	17.6	17.6
Slot body bottom width B_{s1} (mm)	15.75	13.8	10.5
Slot wedge maximum width B_{s2} (mm)	23.75	21.6	17.5

4.1. No-Load Back-EMF

The back-EMF reflects the magnetic field in the ARFTPM machines, and thus the correctness of the electromagnetic field analysis can be verified by analyzing the no-load back-EMF. The no-load characteristics of the ARFTPM machines with different slot numbers are analyzed by 3-D FEA. The no-load back-EMF waveforms and harmonic amplitudes of the ARFTPM machines are obtained in Figure 8.

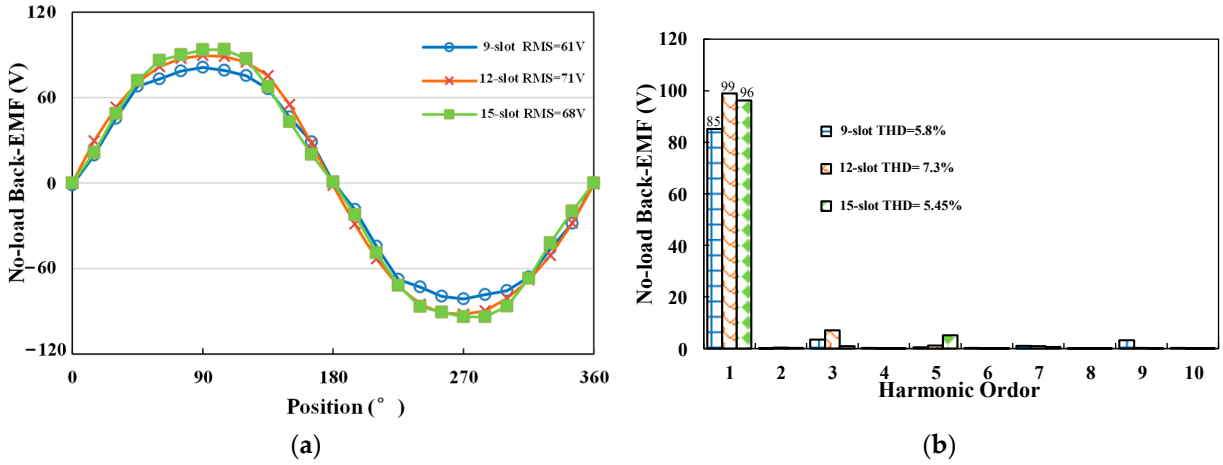


Figure 8. No-load back-EMFs at 250 r/min with only PM (**a**) waveforms; (**b**) spectra.

As shown in Figure 8a, the back-EMFs of three machines are all symmetrical. From Figure 8b, the 12-slot machine has a larger fundamental of back-EMF than the 15-slot, which can be attributed to the higher winding factor K_{wp}, which also proves the higher magnet usage efficiency in the 12-slot machine. Therefore, it can be concluded that the 12-slot machine could provide stronger field regulation capability than the 15-slot machine. The back-EMF effective values of the 12-slot and 15-slot machines are 71 V and 68 V.

Due to the tip leakage reactance of the stator teeth in Figure 5a, the fundamental amplitude of back-EMF in the 9-slot is lower than the 12-slot and 15-slot counterparts. As shown in Table 1, the winding factor of the 15-slot machine is smaller than others, resulting in a lower power density. Furthermore, the back-EMFs are analyzed by a fast Fourier

transform (FFT) method. The total harmonic distortions (THD) formula of back-EMF is as follows [7]:

$$\mathrm{THD} = \frac{\sqrt{\frac{1}{T}\int_{\mathrm{r}} \left(\sum_{n=2}^{\infty} E_n \sin(n\omega t + \alpha_n)\right)^2 dt}}{\sqrt{\frac{1}{T}\int_{\mathrm{r}} \left(E_1 \sin(n\omega t + \alpha_1)\right)^2 dt}} \times 100\% \tag{6}$$

where E_n is the root mean square (RMS) value of the fundamental wave, E_1 is the total RMS value, which can represent current or voltage. The amplitude of the third harmonic is always the largest, which is much higher than other harmonics. The THD are 5.8%, 7.3%, and 5.5% for 9-slot, 12-slot, and 15-slot machines which, demonstrates that the back-EMFs are sinusoidal.

As a result, the amplitude of the harmonic is reduced, and the no-load back-EMF waveform is improved; meanwhile, the magnet usage efficiency of ARFTPM machines is improved by changing the number of slots.

4.2. Cogging Torque

According to the energy method principle, the cogging torque is defined as [17]

$$T_{cog} = -\frac{\partial W_{\mathrm{airgap}}}{\partial \alpha} = -\frac{\partial}{\partial \alpha} \cdot \left[\frac{1}{2\mu_0} \cdot \frac{1}{2}\left(R_2^2 - R_1^2\right) \cdot L_s \cdot \int_0^{2\pi} G^2(\theta) \cdot B^2(\theta)\, \mathrm{d}\theta\right] \tag{7}$$

where W is the magnetic field energy when the motor is not powered. α is the angle between the centerline of a specified tooth and the centerline of a specified PM pole. The PMs of internal HE motors are not directly in contact with the air gap, and the magnetic energy could be negligible, so $W \approx W_{gap}$. μ_0, L_s, R_1, R_2 are vacuum relative permeability, stack length, rotor outer diameter, and stator inner diameter, respectively. $G^2(\theta), B^2(\theta)$ are the functions between relative air gap permeability, air gap flux density, and the relative angle θ of the stator and rotor. The Fourier decomposition of $G^2(\theta), B^2(\theta)$ is given by

$$G^2(\theta) = \sum_{n=0}^{\infty} G_{nZ} \cos nZ\theta \tag{8}$$

$$B^2(\theta, \alpha) = \sum_{n=0}^{\infty} B_{2np} \cos 2np(\theta + \alpha) \tag{9}$$

where G_{nZ} and B_{2np} are the Fourier expansion coefficients of $G^2(\theta)$ and $B^2(\theta)$. Combining Equations (7)–(9), the expression of the cogging torque can be obtained as

$$Y_L = LCM(Z, 2p) \tag{10}$$

$$T_{\mathrm{cog}}(\alpha) = \frac{\pi L_s}{4\mu_0}\left(R_2^2 - R_1^2\right) \cdot \sum_{n=0}^{\infty} nY_L G_{nY} B_{nY} \sin nY_L\alpha \tag{11}$$

From Equation (11), the amplitude of B_{nY}, G_{nY}, and Y_L could be changed to reduce cogging torque, and G_{nY} can be reduced by optimizing the stator slot width and stator tooth shape. Particularly, Y_L can be reduced by choosing the appropriate pole slot combination, and thus T_{cog} will be reduced.

The number of cogging cycles F per slot pitch is defined as [18]

$$F = \frac{\mathrm{LCM}(Z, 2p)}{Z} \tag{12}$$

A higher value of F is preferable as the cogging torque with high LCM exhibits low peak amplitude. Certain design parameters can have a very significant effect on cogging torque, in particular the slot and pole number combination. To demonstrate the influence of slot and pole number combinations on cogging torque, the magnets are fully radially

magnetized throughout their volume. The calculation results of cogging torque are shown in Figure 9.

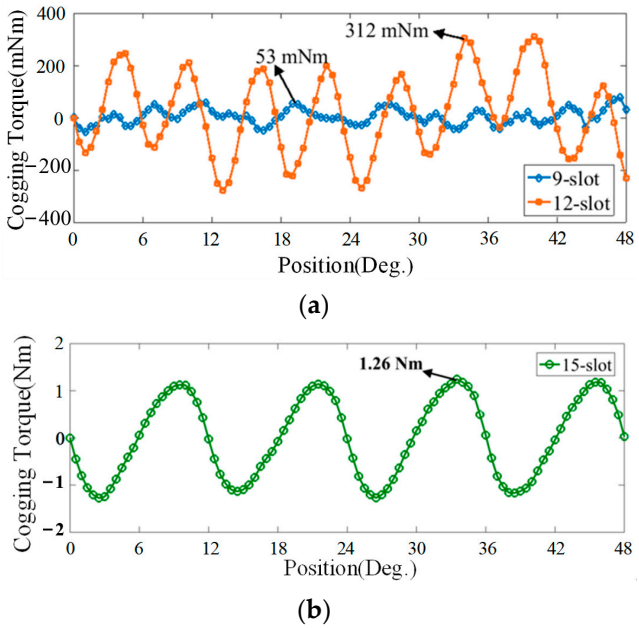


Figure 9. Cogging torque waveforms with only PM (**a**) 9-slot and 12-slot; (**b**) 15-slot.

It should be noted that the cogging torque cycle number per electric period is six in 12-slot machines while it is twelve in 15-slot machines. As shown in Figure 9a, the cogging torque amplitudes of 9-slot and 12-slot ARFTPM machines are 0.053 Nm. and 0.312 Nm., while the cogging torque amplitude of the 15-slot machine is the largest (1.26 Nm.) in Figure 9b. It can be concluded that the cogging torque of the 9-slot ARFTPM machine is lower than the 12-slot and 15-slot counterparts, which can be attributed to the larger LCM in Table 1. Therefore, the no-load characteristics and cogging torque of machines can be optimized by selecting an appropriate slot number; thereby, the output capability of the ARFTPM machine could be improved.

The power angle is of great significance to studying the power changes in ARFTPM machines. At a constant speed, the torque is positively correlated with the power.

The comparison of torque-angle characteristics is shown in Figure 10. When the average torques of the three machines are the same, the angle of the 9-slot ARFTPM machine is higher than the 12-slot and 15-slot with less than 90°. For example, when the torques of three machines are all 10.6 Nm., the angles (Z/p) are 57° (9/5), 35° (12/5), and 48° (15/5), respectively.

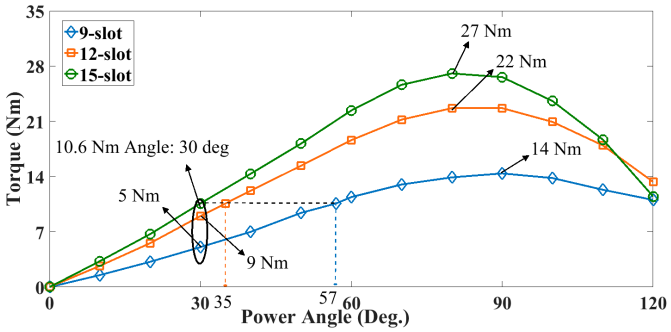


Figure 10. Comparison of torque-angle characteristics.

The torque of the 15-slot machine is larger than that of the 9-slot and 12-slot while the angles are kept the same. For instance, the torques of the machines are 5 Nm. (9/5),

9 Nm. (12/5), and 10.6 Nm. (15/5) when the angles of the three ARFTPM machines are all 30°. Meanwhile, it can be observed that the maximum torque T_{max} of the 15-slot ARFTPM machine is 27 Nm. The results show that the average value of 9-slot machine torque-angle characteristics is the smallest. Combined with the conclusions in Figures 5 and 8, it can be determined that the torque output capacity of 9-slot is decreased due to the decrease in permanent magnet torque.

Since the d-axis synchronous reactance X_d of the ARFTPM machine is generally smaller than the q-axis synchronous reactance X_q, the reluctance torque is a negative sine function. According to Figure 13, the angles corresponding to the average torque maximum value T_{max} of the 9-slot and 12-slot machines are both less than 90°. When the angles of the three machines are larger than 90°, their torques will be decreased with the increasing power angle, and then the machines will enter the unstable operation region.

4.3. Flux Regulation

The flux regulation capability is crucial for ARFTPM machines, and the change in air-gap flux density can be reflected by back-EMF. Therefore, the influence of axial MMF on air gap flux density can be studied through the analysis of back-EMF. The no-load back-EMF of ARFTPM machines with different axial MMFs are analyzed, and the results are shown in Figure 11.

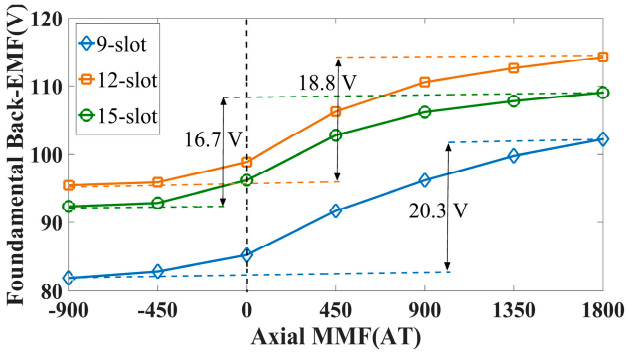


Figure 11. Variation in the back-EMF fundamental amplitude at 250 r/min versus axial MMF.

According to Figure 11, since the saturation of the magnetic shunt, the no-load back-EMF fundamental amplitudes of ARFTPM machines are decreased when the axial MMF changes from 0 AT to −900 AT. The flux-weakening ranges of the three machines are at 3.5 V.

The 9-slot ARFTPM machine has the widest flux regulation range (20.3 V), while the 12-slot and 15-slot counterparts are 18.8 V and 16.7 V, respectively. The flux regulation capability of the 9-slot machine is stronger. The range of flux-enhancing is almost six times that of flux-weakening due to the magnetic saturation. Furthermore, when the axial MMF is 0 AT, the back-EMF fundamental amplitude of the 12-slot machine is larger than the 9-slot. Therefore, it can be concluded that the 12-slot machine is easier to obtain saturated in the flux-enhancing state because of its higher utilization with 0 AT axial MMF.

4.4. Average Torque

Apart from the excellent flux regulation capability, the torque is also a key factor in ARFTPM machines. The variations in the average torque at different axial MMFs are analyzed by 3-D FEA, shown in Figure 12.

According to Figure 12, due to the positive correlation between back-EMF and torque, the torque change trend is like the back-EMF amplitude. The operation states are kept the same to demonstrate the influence of the stator slot number on torque. When the axial MMF is 0 AT, the torques of ARFTPM machines are all 10.6 Nm. The 9-slot ARFTPM machine has larger torque than the 12-slot and 15-slot machines when the axial MMF changes from 0 AT to 1800 AT, and it also has the widest torque improvement range, which is 55.38%.

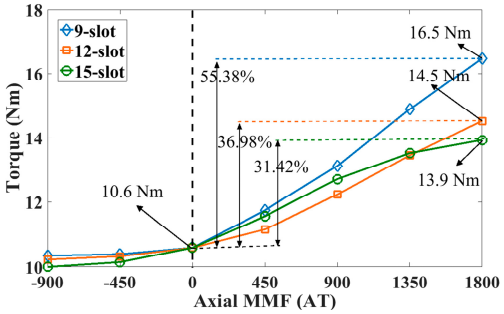


Figure 12. Variation in the average torque versus axial MMF.

4.5. Summary of Electromagnetic Performance

The basic electromagnetic characteristics, including back-EMF, cogging torque, flux regulation capability, and torque of ARFTPM machines, are evaluated and compared, and the results are summarized in Table 5. The 15-slot machine has the lowest back-EMF harmonics and the largest torque, while the 9-slot machine has excellent flux regulation capability and torque performance and the lowest cogging torque.

Table 5. Summary of key performance of the ARFTPM machines.

Performance	9-Slot	12-Slot	15-Slot
Winding coefficient	0.945	0.933	0.866
Back-EMF per turn (V)	61	71	68
Back-EMF amplitude with ±450 AT on FC slots (V)	83~92	96~106	93~103
Back-EMF amplitude with −900~1800 AT on FC slots (V)	82~102	95~114	92~109
Peak cogging (mN.m.)	53	312	1260
Torque maximum (N.m.)	14	22	27
Cogging cycle number	10	5	2

5. Experimental Validation

In order to validate the FEA predictions, the three-phase 12/10 ARFTPM machine prototype is fabricated and measured, and an experimental platform is built for experimental testing, as shown in Figures 13 and 14. To verify the accuracy of the analysis data, the no-load back-EMF was measured with the device. The back-EMF of the armature winding of an ARFTPM is measured by connecting an adjustable DC power supply to the excitation winding. The speed of the prime mover is fixed at the rated speed. When the DC power supply is regulated at this time, the back-EMF will change. The experimental results are shown in Figure 15, indicating the excellent flux regulation capability of the machine. When the axial MMF is 0 AT, the maximum voltage is 180 V, while the minimum value is −178 V, and the RMS value of the voltage is 126 V. When the axial MMF is 1050 AT, the maximum voltage is 194 V, while the minimum value is −192 V, and the RMS value of the voltage is 135 V. As for the simulation data, the RMS value of the phase voltage is 71.5 V when the axial MMF is 0 AT. When the axial MMF is 1050 AT, the RMS value of the phase voltage is 79 V. The RMS changes from 126 V to 130 V and then increases to 134 V and 135 V. This can be seen as a drastic change; the RMS changes by 7% when 126 goes to 135.9. Overall, the relative error between the experimental results and the calculated results is less than 2%, within the reasonable range. The measured data and the calculated results are shown in Table 6.

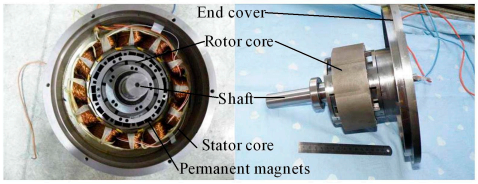


Figure 13. Machine prototype.

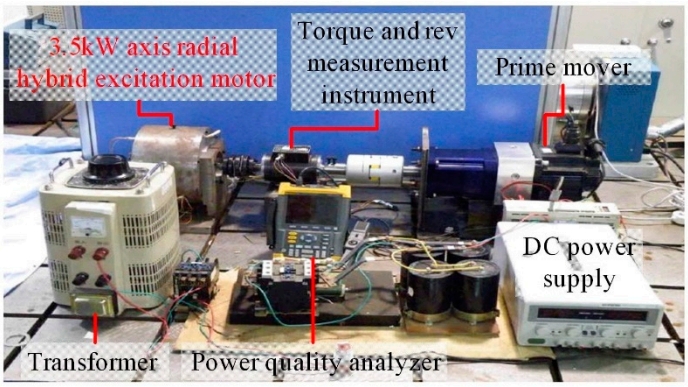


Figure 14. Experimental testing.

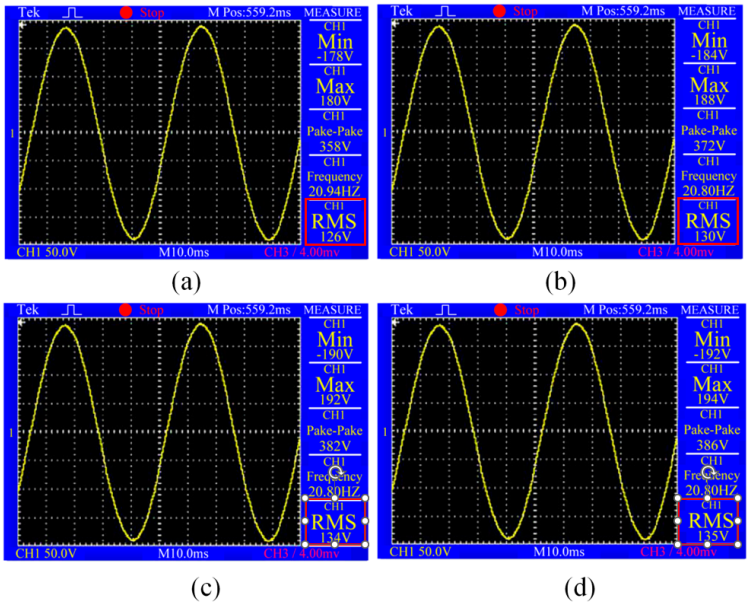


Figure 15. Measured no-load back-EMF waveforms at 250 r/min with different axial MMF of the 12-slot ARFTPM machines (**a**) without axial MMF; (**b**) axial MMF 375 AT; (**c**) axial MMF 750 AT; and (**d**) axial MMF 1050 AT.

Table 6. The comparison of measured data and calculated results at 250 r/min with different axial MMFs of the 12-slot ARFTPM machine.

Excitation Potential (AT)	Phase No-Load Back-EMF (Phase Voltage)	
	Measured Data (V)	Calculated Result (V)
0	73.0	71.5
375	75.9	74.2
750	78.0	77.7
1050	78.8	79.0

6. Conclusions

In this paper, an ARFTPM machine for electric vehicles is taken as the research object, and the electromagnetic field under no-load and load operation is numerically calculated. The flux regulation and torque performance at different slot number machines are comprised and analyzed. The research conclusions are as follows:

1. The decrease in slot number is beneficial to improve the flux regulation capability of the ARFTPM machine, but it also reduces the no-load back-EMF with only PM excitation due to the end region leakage reactance of the teeth. The 9-slot ARFTPM machine has

the best flux regulation capability, and its back-EMF is increased by 24% from −900 AT to 1800 AT, while the back-EMF of the 15-slot is increased by 18%. In addition, the 9-slot machine also has excellent torque improvement, and the torque is increased by 55.38% with axial MMF. However, with only PM excitation, the 9-slot has the lowest back-EMF (60 V), while the back-EMF of the 12-slot is 71 V.

2. When the power angles of machines with different stator slot numbers are the same, the 15-slot ARFTPM machine with only PM excitation has the largest torque, and its maximum torque is 27 Nm., which is twice as large as the 9-slot machine. However, the cogging torque of the 15-slot is the largest due to the lowest F.

Author Contributions: Conceptualization, H.Q. and C.Y.; methodology, R.Y.; validation, R.Y. and W.G.; formal analysis, W.G.; investigation, C.Y.; resources, W.G.; writing—original draft preparation, J.R.; writing—review and editing, C.Y.; supervision, H.Q.; funding acquisition, H.Q. All authors have read and agreed to the published version of the manuscript.

Funding: This work was supported in part by the National Natural Science Foundation of China under Grant 52477066, 52177063; in part by the Excellent Young Scholars Project of Henan Province under Grant 232300421070; in part by the University Science and Technology Innovation Talent Support Program of Henan Province under Grant 23HASTIT026; and in part by the Science and Technology Project of Henan Province under Grants 232102220080, 222102320074, and 242102221002.

Data Availability Statement: The original contributions presented in the study are included in the article; further inquiries can be directed to the corresponding author.

Conflicts of Interest: The authors declare no conflicts of interest.

References

1. Zhang, L.; Fan, Y.; Lorenz, R. Design and analysis of a new five-phase brushless hybrid-excitation fault-tolerant machine for electric vehicles. *IEEE Trans. Ind. Appl.* **2017**, *53*, 3428–3437. [CrossRef]
2. Qiu, H.; Yuan, C.; Chen, W.; Ma, X.; Xiong, B. Combined Regulation Performance Research of the Novel Flux-Torque Regulation Hybrid Excitation Machine with Axial-Radial Magnetic Circuit. *IEEE Trans. Transp. Electrif.* **2022**. [CrossRef]
3. Li, W.; Ching, T.W.; Chau, K.T. A hybrid-excited vernier permanent magnet machine using homopolar topology. *IEEE Trans. Magn.* **2017**, *53*, 1–7. [CrossRef]
4. Wang, J.; Li, H.; Zhou, Y. Design of hybrid excitation flux switching machine based on air-gap field modulation. In Proceedings of the 2021 24th International Conference on Electrical Machines and Systems (ICEMS), Gyeongju, Korea, 31 October–3 November 2021; pp. 1073–1078.
5. Frederick, B. Hybrid Excited Generator with Flux Control of Consequent-Pole Rotor. U.S. Patent 4,656,379, 4 July 1987.
6. Kato, T.; Minowa, M.; Hijikata, H.; Akatsu, K.; Lorenz, R.D. Design methodology for variable leakage flux IPM for automobile traction drives. *IEEE Trans. Ind. Appl.* **2015**, *51*, 3811–3821. [CrossRef]
7. Zhou, X.; Buticchi, G.; Migliazza, G.; Wang, S.; Galea, M.; Gerada, C. Review of speed-extension of permanent magnet synchronous motor with reconfigurable-winding system. In Proceedings of the 2021 IEEE 30th International Symposium on Industrial Electronics (ISIE), Kyoto, Japan, 20–23 June 2021; pp. 1–6.
8. Gong, Y.; Chau, K.T.; Jiang, J.Z.; Yu, C.; Li, W. Analysis of doubly salient memory motors using Preisach theory. *IEEE Trans. Magn.* **2009**, *45*, 4676–4679. [CrossRef]
9. Hua, H.; Zhu, Z.Q.; Hua, W.; Zhu, L.; Jiang, S.; Luo, X. Investigation of partitioned stator hybrid excited switched flux machines with different rotor piece numbers. In Proceedings of the 2019 22nd International Conference on Electrical Machines and Systems (ICEMS), Harbin, China, 11–14 August 2019; pp. 1–5.
10. Wu, Z.; Fan, Y.; Chen, H.; Wang, X. Electromagnetic force and vibration study of dual-stator consequent-pole hybrid excitation machine for electric vehicles. *IEEE Trans Veh. Technol.* **2021**, *70*, 4377–4388. [CrossRef]
11. Qiu, H.; Ran, Y.; Li, W. Influence of rectifiers on highspeed permanent magnet generator electromagnetic and temperature fields in distributed power generation systems. *IEEE Trans. Energy Convers.* **2015**, *30*, 655–662.
12. Orlowska-Kowalska, T. Fault diagnosis and fault-tolerant control of pmsm drives–state of the art and future challenges. *IEEE Access* **2022**, *10*, 59979–60024. [CrossRef]
13. Liu, Y.; Zhang, Z.; Zhang, X. Design and optimization of hybrid excitation synchronous machines with magnetic shunting rotor for electric vehicle traction applications. *IEEE Trans. Ind. Appl.* **2017**, *53*, 5252–5261. [CrossRef]
14. Xu, F. Influence of slot number on Electromagnetic Performance of 2-pole High-Speed Permanent Magnet Motors with Toroidal Windings. *IEEE Trans. Ind. Appl.* **2021**, *57*, 6023–6033. [CrossRef]
15. Geng, H. Performance Optimization Analysis of Hybrid Excitation Generator with the Electromagnetic Rotor and Embedded Permanent Magnet Rotor for Vehicle. *IEEE Access* **2021**, *9*, 163640–163653. [CrossRef]

16. Chau, K.T.; Cheng, M.; Chan, C.C. Nonlinear magnetic circuit analysis for a novel stator doubly fed doubly salient machine. *IEEE Trans. Magn.* **2002**, *38*, 2382–2384. [CrossRef]
17. Lee, S.J.; Kim, S.I.; Hong, J.P. Characteristics of PM Synchronous Motors According to Pole-slot Combinations for EPS Applications. *Int. J. Automot. Technol.* **2014**, *15*, 1183–1187. [CrossRef]
18. Islam, M.S.; Mir, S.; Sebastian, T. Issues in reducing the cogging torque of mass-produced permanent-magnet brushless DC motor. *IEEE Trans. Ind. Appl.* **2004**, *40*, 813–820. [CrossRef]

Disclaimer/Publisher's Note: The statements, opinions and data contained in all publications are solely those of the individual author(s) and contributor(s) and not of MDPI and/or the editor(s). MDPI and/or the editor(s) disclaim responsibility for any injury to people or property resulting from any ideas, methods, instructions or products referred to in the content.